Atmospheric Research 340 (2026) 109070

Contents lists available at ScienceDirect

Atmospheric Research

journal homepage: www.elsevier.com/locate/atmosres

Sustenance characteristics and discriminant method of low-level jets based on coherent Doppler wind lidar

Yue Liu [a,b], Jinlong Yuan [a,b,c,*], Shuo Zhang [a,b], Anning Chen [a,b], Jiadong Hu [a,b], Jiawei Qiu [a,b], Xu Zhou [c], Shuxue Zhou [c], Haiyun Xia [a,b,d], Zhiyuan Jin [e]

[a] State Key Laboratory of Climate System Prediction and Risk Management, Nanjing University of Information Science and Technology, Nanjing 210044, China
[b] School of Atmospheric Physics, Nanjing University of Information Science and Technology, Nanjing 210044, China
[c] CMA Weather Modification Center, Beijing 100081, China
[d] Institute of Lidar Technology, GuangZai Co., Ltd., Hangzhou 310005, China
[e] CAAC Central and Southern Regional Administration, Guangzhou 510405, China

ARTICLE INFO

Keywords:
Coherent Doppler wind lidar
Low-level jet
Aviation safety
Jet sustenance index

ABSTRACT

Strong wind shear induced by low-level jets (LLJs) poses a significant threat to aviation safety. Based on long-term observational data from the Doppler wind lidar at Guangzhou Baiyun International Airport during the period from October 2022 to April 2023, this study systematically investigates the noontime evolution characteristics of LLJs. Through the identification and statistical analysis of 82 LLJ events, the results show that the core height and thickness are the dominant parameters determining LLJ sustenance around noon. Using 5-fold cross-validation and maximizing Youden's J index, optimal thresholds for core height and thickness are determined as 0.90 km and 1.15 km. A Jet Sustenance Index (JSI) is then developed as a discriminant method, achieving an accuracy of 84%. Case analyses further reveal the combined influence of jet structural parameters, the upward development of turbulence, and the persistence of synoptic-scale forcing on LLJ sustenance. These results provide a scientific basis for warnings of wind shear induced by LLJs at airports.

1. Introduction

The low-level jet (LLJ) is a strong, narrow air current characterized by a wind speed maximum in the lower troposphere (Stensrud, 1996). As a widespread atmospheric phenomenon (Rife et al., 2010; Zhang et al., 2006), the strong wind shear associated with LLJs not only triggers boundary layer turbulence and modulates the vertical exchange of heat, moisture, and pollutants (Banta et al., 2006; Darby et al., 2006), but also influences urban heat island intensity (Hu et al., 2013), wind energy resource evaluation (Storm et al., 2009), and the initiation of heavy precipitation (Song et al., 2005). Furthermore, the abrupt wind shear induced by LLJs poses a direct threat to aviation safety during take-off and landing, making it a key concern for aviation meteorological warnings and operational support (Choi and Lee, 2012; Madougou et al., 2013; Shu et al., 2018). Observational studies at Hong Kong International Airport indicate that under the northeasterly monsoon, LLJs can cause sudden headwind changes of 15–20 knots during critical flight phases, thereby significantly increasing the risk of go-arounds and operational hazards (Chan et al., 2020). Therefore, analyzing the characteristics of LLJs is of great importance for aviation flight safety.

The formation mechanisms of LLJs are complex and diverse, primarily including inertial oscillations, topographic baroclinic effects, land-sea thermal contrasts, and synoptic-scale forcing (Blackadar, 1957; Holton, 1967; Li and Chen, 1998; Parish and Oolman, 2010). Based on differences in their formation mechanisms and vertical structures, LLJs are commonly categorized into Boundary Layer Jets (BLJs) and Synoptic-system-related Low-Level Jets (SLLJs) (Chen et al., 1994; Du et al., 2012). BLJs typically occur within the planetary boundary layer at altitudes below 1 km, which are predominantly driven by inertial oscillations and local thermal contrasts, exhibiting a pronounced diurnal cycle with peak intensity in the early morning. In contrast, SLLJs predominantly form at altitudes between 1 and 3 km, closely associated with synoptic-scale systems such as the low-pressure vortices, which show no clear diurnal variation and tend to persist for longer durations (Zheng et al., 2026; Zhou et al., 2026). In recent years, with the widespread application of high spatiotemporal resolution observational

* Corresponding author at: State Key Laboratory of Climate System Prediction and Risk Management, Nanjing University of Information Science and Technology, Nanjing 210044, China.
E-mail address: yuanjinlong@nuist.edu.cn (J. Yuan).

https://doi.org/10.1016/j.atmosres.2026.109070
Received 12 January 2026; Received in revised form 6 May 2026; Accepted 6 May 2026
Available online 7 May 2026

instruments such as wind profilers and lidars, significant progress has been achieved in refined studies of LLJs over typical regions of China (Miao et al., 2018; Su et al., 2024; Ding et al., 2025). In particular, a number of studies have focused on LLJs in South China, investigating their climatology, interactions with weather systems, and roles in heavy rainfall (Du and Chen, 2018, 2019; Li and Du, 2021; Luo and Du, 2025). These studies have laid a foundation for a deeper understanding of the multi-scale impacts of LLJs. However, current research at major airports has focused primarily on the detection and analysis of low-level wind shear (Li et al., 2020; Zhang et al., 2019), while detailed investigations into the evolution of LLJs, a key trigger of wind shear, remain relatively scarce.

Guangzhou city is located in a high-frequency region for LLJs along the South China coast (Yan et al., 2021). Local LLJs are primarily modulated by the interplay between the subtropical monsoon circulation and land-sea thermal contrasts, with a higher occurrence from October to December and from February to April (Miao et al., 2018). As one of the busiest aviation hubs in China, Guangzhou Baiyun International Airport ranks among the top airports nationwide in terms of annual passenger throughput, making aviation safety a critical priority. The sudden wind shear induced by LLJs is a key meteorological factor threatening aircraft takeoff and landing operations at the airport. During the observation period, eight wind shear events were reported at the airport. Four events were primarily attributed to boundary layer turbulence and typhoon, and four events, constituting half of the total, were directly associated with LLJs. Notably, all four LLJ-related events occurred during the noontime period (11,00–13,00 BJT). Based on concurrent Coherent Doppler Wind Lidar (CDWL) observations, full-time data screening revealed a marked divergence in LLJ evolution during this window: some jets maintained their structure, while others dissipated rapidly, and the majority of sustenance and interruption decisions were confirmed to occur within this time window. Previous studies on the diurnal variations of LLJs have thoroughly investigated their formation mechanisms and diurnal characteristics, consistently finding that LLJs occur more frequently during early morning and evening, with occurrence frequencies dropping significantly around noon (Dong et al., 2021; Du et al., 2012). Noontime presents a critical transition period for LLJ evolution, as surface heating promotes the development of the convective mixed layer and enhances turbulent mixing, which in turn influences jet sustenance. This time window also coincides with one of the airport's peak periods for flight take-offs and landings, making the clarification of LLJ sustenance at noon valuable for aviation wind shear warnings.

This study leverages CDWL observations to investigate the statistical characteristics and physical mechanisms governing the noontime evolution of LLJs. The key parameters governing the noontime sustenance of LLJs are first identified, followed by the construction of a discriminant method based on the Jet Sustenance Index (JSI). Finally, the noontime evolutionary processes of typical and special cases are analyzed. The paper is structured as follows: Section 2 describes the data sources and methodology. Section 3 analyzes LLJ characteristic parameters. Section 4 develops the discriminant method. Section 5 presents physical mechanism analyses of BLJ and SLLJ cases, each including typical and atypical events. Section 6 summarizes the main conclusions and proposes future research directions.

2. Data and methods

2.1. Site and instrument

This study employs wind profile data from the CDWL at Guangzhou Baiyun International Airport (23.3925°N, 113.2989°E) from October 2022 to April 2023. Guangzhou Baiyun Airport is one of the busiest airports in China, located in the Pearl River Delta Plain, featuring terrain that is slightly higher in the north and gentler in the south (Fig. 1a). The CDWL employed in this study (Fig. 1c) was installed at the location marked by a red triangle within the airport observation field (Fig. 1b). The lidar operates at an eye-safe wavelength of 1.5 μm, with a spatial resolution of 30 m and a temporal resolution of 1 s. Detailed parameters and its applications are described in Xia et al. (2024). During the experimental period, the lidar operated in the Velocity Azimuth Display (VAD) scanning mode with an elevation angle of 60° and an azimuthal scanning range of 0°-180°, enabling effective detection of low-level wind field information (Yuan et al., 2020).

2.2. ERA5 reanalysis data

The ERA5 dataset, provided by the European Centre for Medium-Range Weather Forecasts (ECMWF), is a global meteorological reanalysis dataset. It is generated using advanced numerical weather prediction techniques, based on extensive observational data and numerical weather prediction models. The ERA5 dataset has a spatial resolution of 0.25° × 0.25° and a temporal resolution of hourly. It covers multi-level atmospheric data from the sur-face to high altitudes. This study selected reanalysis data incorporating meteorological elements such as horizontal wind fields, temperature, and geopotential height.

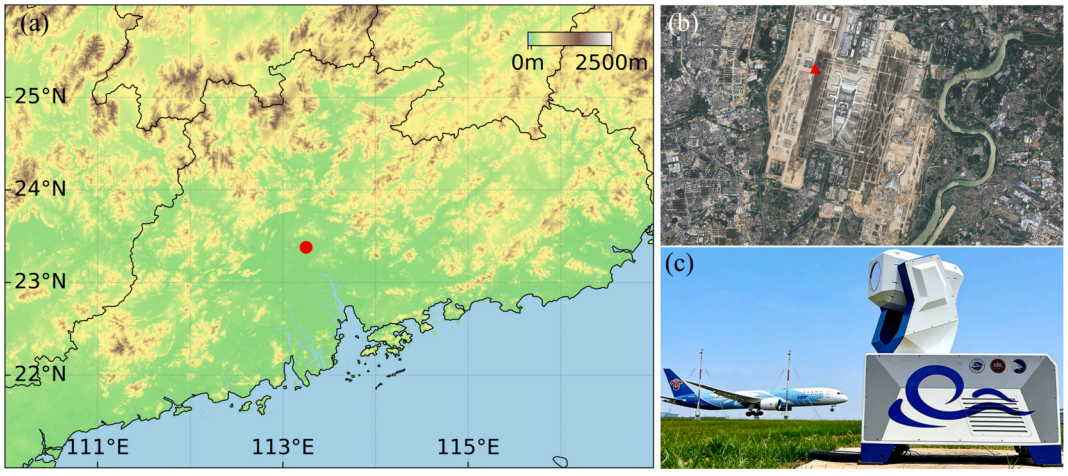

Fig. 1. (a) Topographic map of the Guangzhou region. The red solid circle indicates the location of Guangzhou Baiyun International Airport. (b) Aerial view of Guangzhou Baiyun International Airport. The red triangle marks the installation site of the lidar. (c) Photograph of the CDWL. (For interpretation of the references to colour in this figure legend, the reader is referred to the web version of this article.)

2.3. LLJ Identification and parameter definitions

For the objective identification of LLJ events from continuous observations, diagnostic criteria are developed by integrating common identification standards with the statistical features of local data (Bonner, 1968; Du et al., 2012). LLJ identification is based on the following three criteria: (1) a maximum horizontal wind speed of at least 10 m s^{-1} below 3 km; (2) a minimum duration of 2 h; and (3) a vertical wind shear within the 3 km layer where the wind speed decreases by at least 5 m s^{-1} from its maximum to its minimum value, or the absence of a clear minimum within that layer.

To capture the overall noontime sustenance status, the LLJ events are further classified into two categories based on their behavior during the noontime period, defined as 11:00–13:00 (BJT). Events are classified as interrupted LLJs if the maximum horizontal wind speed at their core remained below 10 m s^{-1} for a cumulative duration of one hour or longer. Conversely, events are classified as sustained LLJs if the core wind speed remained at or above 10 m s^{-1} for the entire period, or if any episodes below this threshold totaled less than one hour, indicating that the primary jet structure was maintained. For cases with cumulative duration near one hour threshold or with oscillations near 10 m s^{-1}, manual verification was conducted to ensure classification accuracy.

From a physical perspective, the sustenance of the LLJ depends on its structural stability and external environmental disturbances. The differences between the two categories are characterized using four key parameters: core height, thickness, maximum wind speed, and turbulence intensity. Core height and thickness directly reflect the vertical structure of the LLJ, with core height commonly used to distinguish different types of LLJs (Du et al., 2012). Maximum wind speed represents the momentum intensity of the jet and is a core criterion in the classical definition of LLJs (Bonner, 1968). Turbulence intensity, as a key external environmental parameter, quantifies the level of turbulent mixing that acts as a disturbance affecting LLJ sustenance. In this study, the core height is the altitude corresponding to this maximum wind speed. The thickness is the average vertical extent where the wind speed continuously remains at or above 10 m s^{-1} during the pre-noon period. The maximum wind speed is defined as the peak horizontal wind speed within the jet core region during the pre-noon period. Turbulence intensity is quantified by the turbulent kinetic energy dissipation rate (TKEDR), estimated from CDWL radial wind data using the azimuth structure function method (Banakh et al., 2021; Banakh and Smalikho, 2018; Wang et al., 2021). For analysis, log10(TKEDR) is first calculated to compress its wide dynamic range onto a linear scale, then vertically averaged over 0–1 km to represent the bulk turbulence intensity within the boundary layer. A high value indicates strong turbulence, and a low value indicates weak turbulence. All four parameters are derived from CDWL observations.

3. Statistical analysis of LLJ parameters

3.1. Parameter characteristics of LLJs

Based on the wind profile data and the established LLJ criteria, a total of 82 LLJs were identified. These events were categorized into sustained LLJs (50 cases) and interrupted LLJs (32 cases). For each category, the four characteristic parameters were analyzed: core height, thickness, maximum wind speed, and log10(TKEDR). The distribution patterns of each parameter were first visualized using kernel density estimation (KDE) curves, as shown in Fig. 2. The results reveal a clear separation in the distributions of core height and thickness between sustained and interrupted LLJs. The distribution for sustained LLJs is shifted toward higher values, indicating that they generally possess a greater core height and a thicker vertical structure. The maximum wind speed distributions also show separation between the two categories, though with considerable overlap. In contrast, the distribution curves for log10(TKEDR) are highly overlapping with only a slight offset, indicating its limited ability to distinguish between the two LLJ types.

To further quantify the distributional differences, a Mann-Whitney *U* test was applied for intergroup comparison. This nonparametric method does not assume a normal data distribution and evaluates median differences by comparing rank sums. Statistical significance was assessed through *p*-values, which quantify the probability of observing the measured differences under the null hypothesis of no group distinction. A significance threshold of $p < 0.01$ was adopted. To evaluate the practical magnitude of the observed differences, the effect size was calculated as the rank-biserial correlation coefficient (r)(Cohen, 1977). An $|r| \geq 0.5$ indicates a large effect size, representing a difference with practical discriminatory significance. Table 1 summarizes the median and interquartile range (IQR, expressed as [Q1, Q3]) for each parameter, which characterize the central tendency and dispersion of the data.

As shown in Table 1, the median values of core height, thickness, and maximum wind speed are all significantly greater for sustained LLJs

Table 1
Results of the Mann-Whitney *U* test.

Parameter	Interrupted Group Median [IQR]	Sustained Group Median [IQR]	p-Value	Effect size(r)
Core Height (km)	0.56 [0.47, 0.78]	1.27 [0.98, 1.53]	3.42e-9	0.65
Thickness (km)	0.70 [0.47, 0.94]	1.78 [1.18, 2.48]	1.34e-8	0.63
Max Wind Speed (m s^{-1})	13.90 [12.12, 15.90]	18.15 [15.58, 20.70]	1.90e-6	0.53
log10(TKEDR) (m^2 s^{-3})	−3.16 [−3.78, −2.92]	−2.78 [−3.28, −2.57]	4.30e-3	0.32

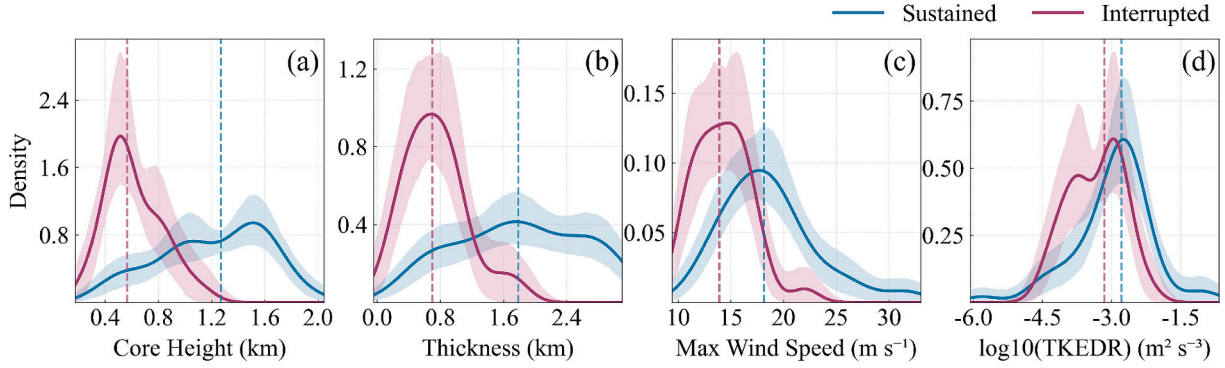

Fig. 2. Kernel density estimation curves for individual parameters. (a) Core height; (b) Thickness; (c) Maximum wind speed; (d) log10(TKEDR). The dashed lines indicate the median positions. The solid lines represent the KDE estimates, and the shaded areas denote the 95% confidence intervals. The dashed lines indicate the median positions.

than for interrupted LLJs. Furthermore, the IQR ranges for these three parameters are wider in sustained LLJs. The effect size analysis shows that core height ($r = 0.65$), thickness ($r = 0.63$), and maximum wind speed ($r = 0.53$) all exhibit large effect sizes. This confirms that the differences in these parameters between sustained and interrupted LLJs are not only statistically significant but also practically substantial. Although the log10(TKEDR) also reaches statistical significance ($p = 0.0043$), its effect size is small ($r = 0.32$). This is consistent with the highly overlapping KDE curves shown in Fig. 2, indicating that the magnitude of difference in log10(TKEDR) between the two groups is relatively limited and that it has weak discriminatory power when used alone.

To explore the correlations among parameters, a matrix of scatter plots for each pair of parameters is constructed as shown in Fig. 3. The analysis reveals positive pairwise correlations among core height, thickness, and maximum wind speed. Sustained LLJs are predominantly concentrated in the high-value regions of these parameter pairs, forming distinct clusters, while interrupted LLJs are largely located in the low-value regions. The two event types exhibit overall separation along the diagonal, with sustained LLJs clustering in the upper-right quadrant and interrupted LLJs clustering in the lower-left quadrant. However, in scatter plots combining log10(TKEDR) with any other parameters, the points of the two LLJ types are extensively intermixed, without forming a clear separation boundary based on turbulence intensity. This indicates that the influence of turbulence on LLJ evolution is likely more complex, being jointly modulated by synoptic system configuration, local stability conditions, and coupled turbulence-jet shear processes.

3.2. Characteristic differences between BLJs and SLLJs

The analysis above indicates that core height, thickness, and maximum wind speed are key factors influencing the noontime state of LLJs, with higher values corresponding to a greater probability of LLJ sustenance. To place these statistical findings within a clearer physical framework and verify their consistency with LLJ formation mechanisms, the classification method is adopted (Du et al., 2012), using a 1 km altitude threshold to classify LLJs. Jets with a core height below 1 km are defined as BLJs, while those with a core height between 1 and 3 km are classified as SLLJs. Fig. 4a presents a bar chart comparing the counts of noontime evolution types for BLJs and SLLJs. Among the 43 BLJ events, 30 (69.8%) were interrupted at noon, while 13 (30.2%) were sustained. In contrast, among the 39 SLLJ events, 37 (94.9%) were sustained, with only 2 (5.1%) interrupted. These results confirm the classical understanding that BLJs, regulated by boundary layer turbulence and thermal processes, often dissipate in the afternoon (Chen et al., 1994). However, the fact that 30.2% of BLJs were sustained at noon indicates that afternoon dissipation is not absolute, and the associated abrupt wind shear can still pose a risk to aviation safety.

Fig. 4b-d display the distribution characteristics of thickness, maximum wind speed, and log10(TKEDR) using boxplots. For thickness (Fig. 4b), the box for interrupted LLJs is generally lower and predominantly consists of BLJ points. The box for sustained LLJs is positioned higher and contains only a few BLJ points, which exhibit significantly greater thickness than interrupted BLJs. The sustained box is largely covered by SLLJ points; even the few interrupted SLLJ cases lie above the overall thickness range of BLJs. Maximum wind speed (Fig. 4c) shows a similar distribution pattern, the few sustained BLJs have higher wind speeds than most interrupted BLJs, suggesting that greater momentum helps counteract turbulent dissipation. The distribution of log10(TKEDR) is distinctly different (Fig. 4d). Although the median of the sustained box is slightly higher, the box ranges of the two groups largely overlap. BLJ and SLLJ points are intermixed without clear separation by type.

In summary, BLJs and SLLJs differ markedly in their physical attributes and noontime evolution. BLJs generally exhibit a shallow and weak-wind profile, and their sustenance depends on increased thickness, enhanced wind speed, and a weaker turbulence environment. In contrast, SLLJs typically possess a deep and strong-wind structure. Sustenance is the norm for SLLJs, and their robust structural and momentum advantages enable them to persist.

4. Development of sustenance discriminant method

Although BLJs and SLLJs differ in their physical origins and structural characteristics, and statistics show distinct patterns in their noontime evolution, real-time and accurate determination of jet type and its noontime state remains challenging for operational forecasting. Therefore, establishing an objective discriminant criterion based on directly observable parameters is of practical value for rapid warning of LLJ noontime sustenance.

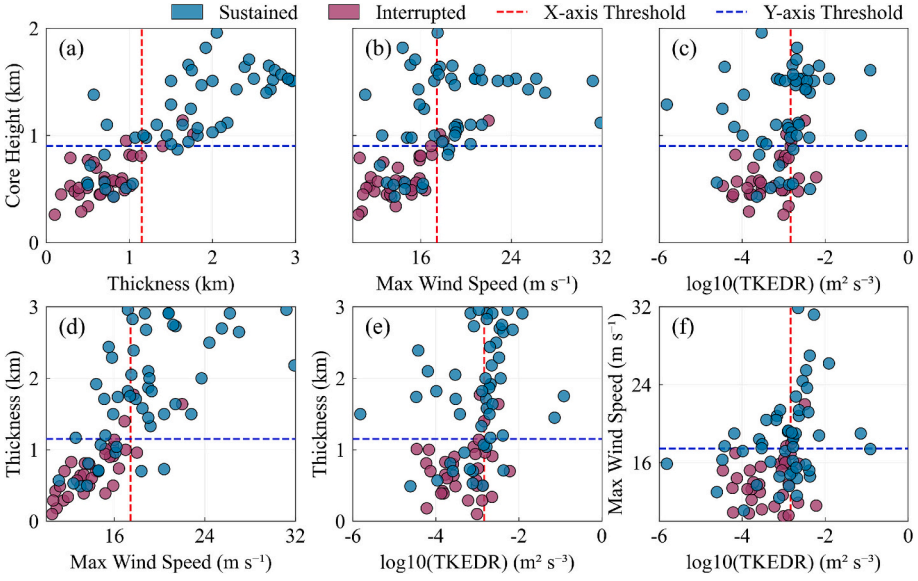

Fig. 3. (a-f) Scatter plots showing the pairwise relationships between the four characteristic parameters of LLJs: core height, thickness, maximum wind speed, and log10(TKEDR). The dashed lines in each subplot represent the mean optimal discrimination thresholds for the corresponding parameters, determined by maximizing Youden's J index.

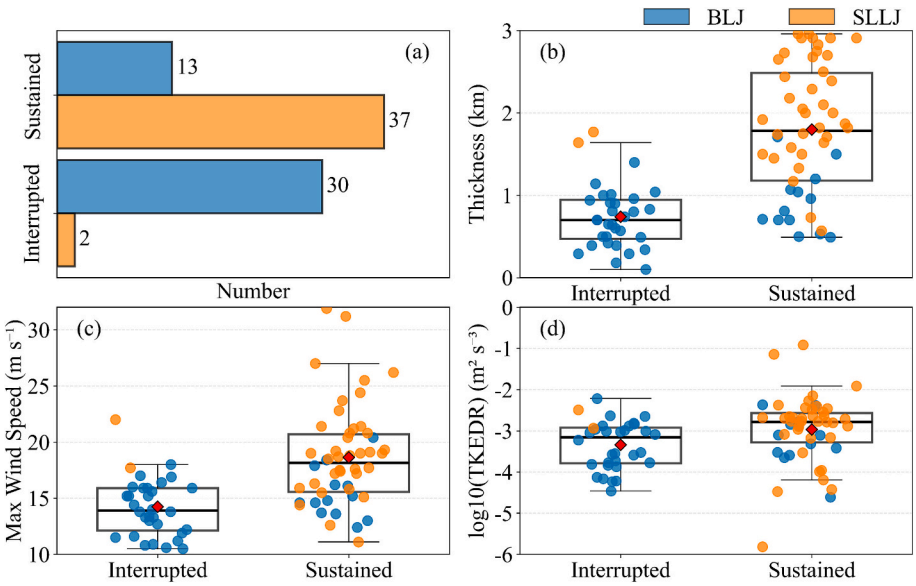

Fig. 4. (a) Bar chart showing the count of sustained and interrupted events for BLJs and SLLJs; (b-d) Boxplots comparing the characteristic distributions of BLJs (blue) and SLLJs (orange). In the boxplots, red diamonds represent the means, while the central line within each box represents the median. The box limits indicate the interquartile range (IQR, from the 25th to the 75th percentile), and the whiskers extend to 1.5 times the IQR from the box hinges. (For interpretation of the references to colour in this figure legend, the reader is referred to the web version of this article.)

To avoid overfitting and evaluate the generalization ability of the method, a stratified 5-fold cross-validation was employed. The 82 LLJ events were randomly partitioned into five folds while preserving the original proportion of sustained and interrupted cases in each fold. In each iteration, approximately 80% of the data were used as the training set to determine the optimal thresholds and weights by maximizing Youden's J index, and the remaining 20% were used as the test set to compute the performance metrics. The final reported thresholds and all metrics are presented as the mean ± standard deviation over the five test folds, reflecting the stability and reliability of the method.

4.1. Evaluation metrics

To quantitatively evaluate the performance of individual parameters and the integrated method, a set of metrics derived from the confusion matrix is employed. The core parameters are defined as follows: True Positives (TP, sustained LLJs correctly identified as sustained), True Negatives (TN, interrupted LLJs correctly identified as interrupted), False Positives (FP, interrupted LLJs incorrectly identified as sustained), and False Negatives (FN, sustained LLJs incorrectly identified as interrupted). The formulas and physical interpretations of the evaluation metrics are as follows(Anuruddhika et al., 2025; Borna and Rahman, 2024; Miao and Zhu, 2022):

True Positive Rate (TPR) / Recall: The probability of correctly identifying sustained events, reflecting the method's detection capability for sustenance.

$$TPR = Recall = \frac{TP}{TP + FN} \tag{1}$$

False Positive Rate (FPR): The probability of incorrectly classifying an interrupted event as sustained, reflecting the risk of false alarms.

$$FPR = \frac{FP}{FP + TN} \tag{2}$$

Accuracy: The overall probability of correct classification, reflecting the general reliability of the discriminant.

$$Accuracy = \frac{TP + TN}{TP + TN + FP + FN} \tag{3}$$

Precision: The probability that an event predicted as sustained is truly sustained, reflecting the reliability of sustained predictions.

$$Precision = \frac{TP}{TP + FP} \tag{4}$$

Specificity: The probability of correctly identifying interrupted events, reflecting the method's ability to correctly classify interrupted events.

$$Specificity = \frac{TN}{TN + FP} \tag{5}$$

Negative predictive value (NPV): The probability that an event predicted as interrupted is truly interrupted, reflecting the reliability of interrupted predictions.

$$Negative\ predictive\ value = \frac{TN}{TN + FN} \tag{6}$$

F1-Score: The harmonic mean of Precision and Recall, balancing the risks of false positives and false negatives.

$$F1 - Score = 2 \times \frac{Precision \times Recall}{Precision + Recall} = 2 \times \frac{TP}{2TP + FP + FN} \tag{7}$$

Youden's J Index: A core metric for evaluating the discriminatory power of a threshold, ranging from [−1,1]. A higher value indicates better performance and serves as the key criterion for optimal threshold selection.

$$Youden's\ J = TPR - FPR \tag{8}$$

4.2. Determination of single parameter thresholds

A discriminant criterion based on directly observable parameters was established by combining ROC curve analysis with Youden's J index optimization and validating feature importance using a Random Forest model. The ROC curve plots the FPR against the TPR. The area under the ROC curve (AUC) represents the overall discriminatory power of a classifier, with values closer to 1 indicating stronger performance. The optimal discrimination threshold for each parameter was determined by maximizing Youden's J index (Eq. 8) (Schisterman et al., 2008). The ROC curve analysis based on 5-fold cross-validation (Fig. 5a) confirms

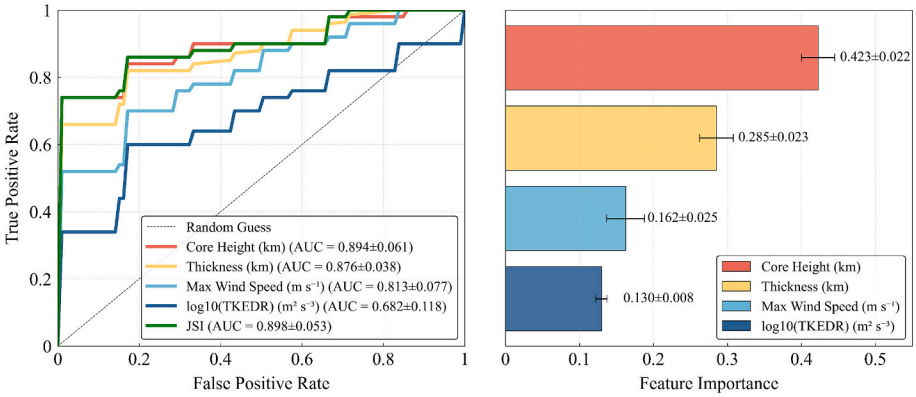

Fig. 5. (a) ROC curves for individual parameters and the integrated method (JSI). (b) Feature importance ranking from the Random Forest model.

the strong discriminatory power of core height (AUC = 0.894 ± 0.061) and thickness (AUC = 0.876 ± 0.038), followed by maximum wind speed (AUC = 0.813 ± 0.077) and log10(TKEDR) (AUC = 0.682 ± 0.118). By maximizing Youden's J index in each training fold, the optimal thresholds were determined as: core height = 0.90 ± 0.05 km, thickness = 1.15 ± 0.06 km, maximum wind speed = 17.44 ± 0.48 m s^{-1}, and log10(TKEDR) = −2.83 ± 0.03 m^2 s^{-3}. These mean thresholds are indicated by dashed lines in the scatter plot matrix (Fig. 3) to visually demonstrate their separation effect.

Concurrently, feature importance was assessed using a Random Forest model. The model was configured with 100 decision trees and a maximum depth of 5 to balance model complexity and overfitting (Breiman, 2001). Sensitivity experiments by varying the number of trees (50–300) and maximum depth (3−10) showed stable discriminative performance and highly consistent feature importance rankings, with core height and thickness consistently the top two features. As shown in Fig. 5b, the feature importance ranking is: core height, thickness, maximum wind speed, and log10(TKEDR), confirming that core height and thickness are the decisive factors for discriminating noontime LLJ sustenance, while turbulence intensity contributes minimally.

4.3. Development of the jet sustenance index (JSI)

To fully leverage the synergistic discriminatory potential of core height (H) and thickness (T), a linear weighted discriminant method was further developed within the same 5-fold cross-validation framework. In each fold, the training set was used to calculate the mean and standard deviation of H and T for *Z*-score standardization using the following formula:

$$H' = \frac{H - \mu_H}{\sigma_H}, T' = \frac{T - \mu_T}{\sigma_T} \quad (9)$$

where μ_H and μ_T are the sample means, and σ_H and σ_T are the sample standard deviations of core height and thickness. After five folds, the mean standardization parameters were obtained: μ_H = 0.98 km, σ_H = 0.45 km, μ_T = 1.38 km, and σ_T = 0.84 km. The standardized features are denoted as $H'$and T'. To comprehensively characterize the noontime sustenance capability of LLJs, the Jet Sustenance Index (JSI) is defined as:

$$JSI = w_1 \times H' + w_2 \times T' \quad (10)$$

where $H'$and $T'$are the standardized core height and thickness, and $w_1$and w_2 are their corresponding weights, satisfying $w_1 + w_2 = 1$.The optimal weights were also determined using the same cross-validation framework. In each fold, all possible weight combinations were systematically traversed with a step size of 0.01, and Youden's J index was maximized on the training set to select the optimal weights and the corresponding JSI threshold. After five folds, the average optimal weights were obtained: w_1 = 0.64 and w_2 = 0.36. Under these average weights, the corresponding optimal JSI threshold was determined by maximizing Youden's J index in each training fold, and the average value over the five folds was −0.14. An LLJ is classified as sustained if JSI≥-0.14, and interrupted otherwise.

The cross-validated performance of all four individual parameters and the JSI, evaluated on the independent test folds, is summarized in Table 2. All metrics are reported as the mean (standard deviation, STD) over the five test folds, comprehensively reflecting both the central tendency and stability of the estimates. The JSI achieves globally optimal forecasting performance, with recall increasing to 80%, accuracy reaching 84%, and the F1-score improving to 0.86, while the false positive rate decreases to 9.5%. Compared with any individual parameter threshold, the JSI provides improved forecasting performance, demonstrating that the synergistic combination of core height and thickness enhances forecast reliability.

5. Mechanistic analysis of case studies

The discriminant thresholds and the JSI derived from statistical patterns require verification and interpretation through physical mechanisms. To this end, representative LLJ events are examined by integrating lidar-observed vertical profiles with reanalysis data, aiming to elucidate the distinct noontime evolution mechanisms of BLJs and SLLJs.

Table 2
Optimal thresholds and cross-validated discrimination performance of individual parameters and the JSI.

Metrics (Mean (STD))	Core Height (km)	Thickness (km)	Max Wind Speed (m s^{-1})	log10 (TKEDR) (m^2 s^{-3})	JSI
Threshold	0.90 (0.05)	1.15 (0.06)	17.44 (0.48)	−2.83 (0.03)	−0.14 (0.09)
Recall	0.780 (0.117)	0.740 (0.049)	0.560 (0.162)	0.460 (0.049)	0.800 (0.063)
FPR	0.153 (0.091)	0.162 (0.183)	0.091 (0.117)	0.809 (0.189)	0.095 (0.078)
Accuracy	0.804 (0.075)	0.780 (0.053)	0.696 (0.134)	0.354 (0.100)	0.840 (0.052)
Precision	0.890 (0.061)	0.898 (0.101)	0.893 (0.132)	0.478 (0.091)	0.933 (0.055)
NPV	0.724 (0.117)	0.668 (0.053)	0.581 (0.114)	0.166 (0.150)	0.745 (0.076)
Specificity	0.847 (0.091)	0.838 (0.183)	0.909 (0.117)	0.191 (0.189)	0.905 (0.078)
F1-Score	0.826 (0.074)	0.806 (0.031)	0.681 (0.158)	0.467 (0.066)	0.860 (0.045)

5.1. Analysis of BLJ events

On February 20, 2023, a typical BLJ was observed by lidar (Fig. 6a1-e1). This jet formed in the early morning and exhibited a shallow structure, with a core height of 0.49 km, a thickness of 0.74 km, and a maximum wind speed of 16.4 m s^{-1}. Before 08:00, the jet core was located near 500 m, with wind speeds exceeding 15 m s^{-1}. During this period, log10(TKEDR) values were relatively high below 500 m but remained low between 500 m and 1 km, indicating that turbulent mixing had not yet extended upward. Richardson number (Ri) analysis (Fig. 6e1) revealed that after 08:00, Ri rapidly decreased to negative values, and the low-Ri region extended vertically to 500 m, marking a transition to convection-dominated thermal turbulence driven by surface heating. Concurrently, the vertical extent of log10(TKEDR) expanded, with strong turbulence extending from below 500 m to approximately 1 km (Fig. 6d1), fully encompassing the jet core. As a result, the wind profile changed markedly: the jet core around 500 m dissipated, wind speeds generally decreased to below 5 m s^{-1}, and the wind direction shifted from persistent northerly to disorganized. The JSI calculated for this event was −0.97, well below the sustenance threshold of −0.14, consistent with the observed interruption.

Although statistics indicate a high probability of BLJ interruption at noon, a few sustained cases were still observed. The BLJ observed on December 5, 2022, serves as a representative example (Fig. 6a2-e2). This BLJ had a core height of only 0.51 km and a maximum wind speed of 16.1 m s^{-1}, but its thickness reached 0.96 km, exceeding the median thickness of interrupted BLJs. Concurrently, the noontime log10(TKEDR) was −3.31 (m^2 s^{-3}), which is lower than that of most BLJ cases, indicating a weaker turbulent environment. Its JSI was −0.85, leading the method to classify it as interrupted, but the observations contradicted this. As shown in Fig. 6a2-e2, the jet structure remained relatively intact around noon. Ri analysis (Fig. 6e2) revealed that after 08:00, Ri also decreased to negative values, which was similar to the February 20 case. However, the critical distinction is that the thermal turbulence remained confined below 200 m and failed to develop upward. This indicates that despite strong thermal instability in the lower layers, the vertical development of turbulence was inhibited, limiting its vertical reach. Consequently, the turbulent mixing did not impinge upon the jet core layer. Although the wind speed at the jet core decreased slightly, it remained above 10 m s^{-1}, and the wind speed gradient structure was not completely eroded by mixing.

In the interrupted case, thermal turbulence developed upward and fully encompassed the core, leading to dissipation. In the sustained case, despite similar thermal instability in the lower layers, thermal turbulence remained confined below the core, allowing the jet to persist. The JSI, which is based solely on core height and thickness, misclassified the sustained case as interrupted because its core height fell below the optimal threshold, while its greater thickness and weaker turbulence environment were insufficient to offset this.

5.2. Analysis of SLLJ events

On January 24, 2023, a typical SLLJ was captured by lidar (Fig. 7a1-e1). The jet exhibited a deep and strong-wind structure, with a core height of 1.51 km, a vertical thickness of up to 2.0 km, and a peak wind speed of 23.7 m s^{-1}. During the observation period, active vertical motions were recorded, with a maximum updraft of 2.30 m s^{-1} and a vertical velocity variance of 0.22 m^2 s^{-2}. The jet core remained stable near 1.5 km altitude, showing no significant wind speed attenuation and maintaining a steady northerly wind direction. Turbulence intensity was notably high and vertically extensive throughout the day, with the region of strong turbulence extending upward to approximately 1.5 km, substantially overlapping with the jet core layer (Fig. 7d1). Analysis of the log10(TKEDR) and Ri (Fig. 7d1, e1) reveals that below 1 km, Ri remained consistently below 0.25, identifying this layer as the primary region for shear-generated turbulence. Above 1 km, Ri gradually increased to approximately 1, indicating stable stratification; nevertheless, log10(TKEDR) remained strong, indicating that turbulence was generated by the strong wind shear associated with the jet itself. Although Ri occasionally became negative below 500 m, indicating thermal instability, its vertical development was limited and did not reach the SLLJ core. The JSI for this structure was 1.01, predicting sustenance, which is consistent with the observations.

Synoptic analysis for that day (Fig. 8a-c) revealed persistently tightly

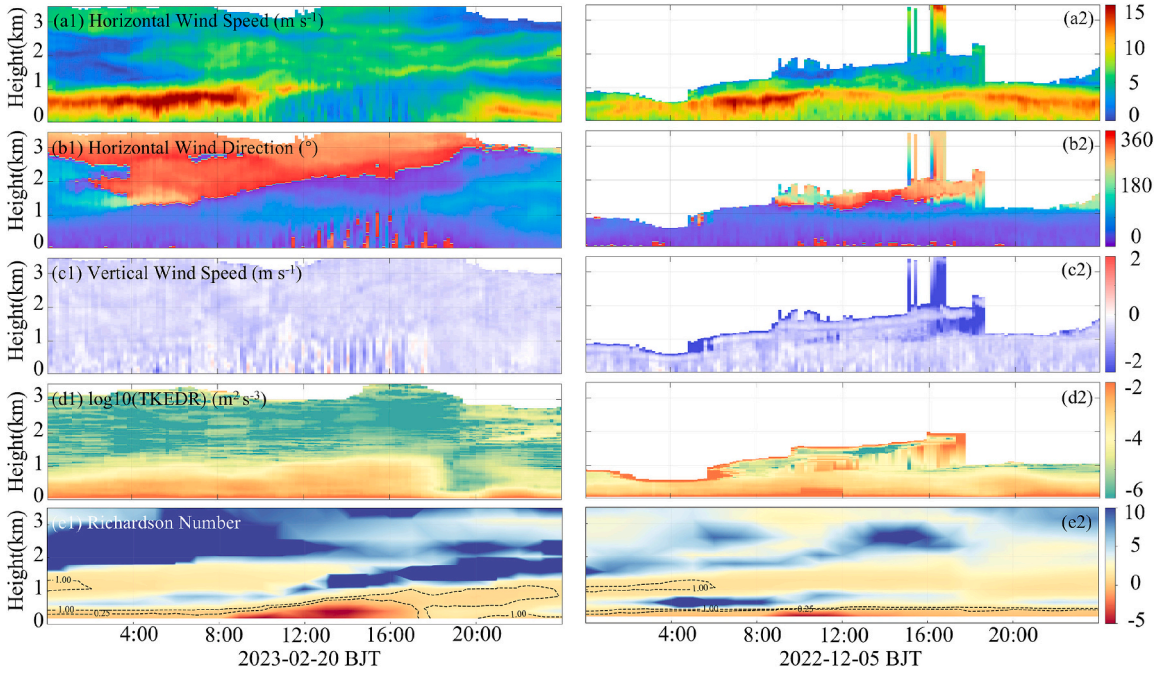

Fig. 6. (a1-e1) The interrupted BLJ case on February 20, 2023; (a2-e2) The sustained BLJ case on December 5, 2022. Panels (a-d) show CDWL observations: (a) Horizontal wind speed (m s^{-1}); (b) Horizontal wind direction (°); (c) Vertical wind speed (m s^{-1}); (d) log10(TKEDR) (m^2 s^{-3}). Panels (e) display the gradient Richardson number (Ri) derived from ERA5 reanalysis data.

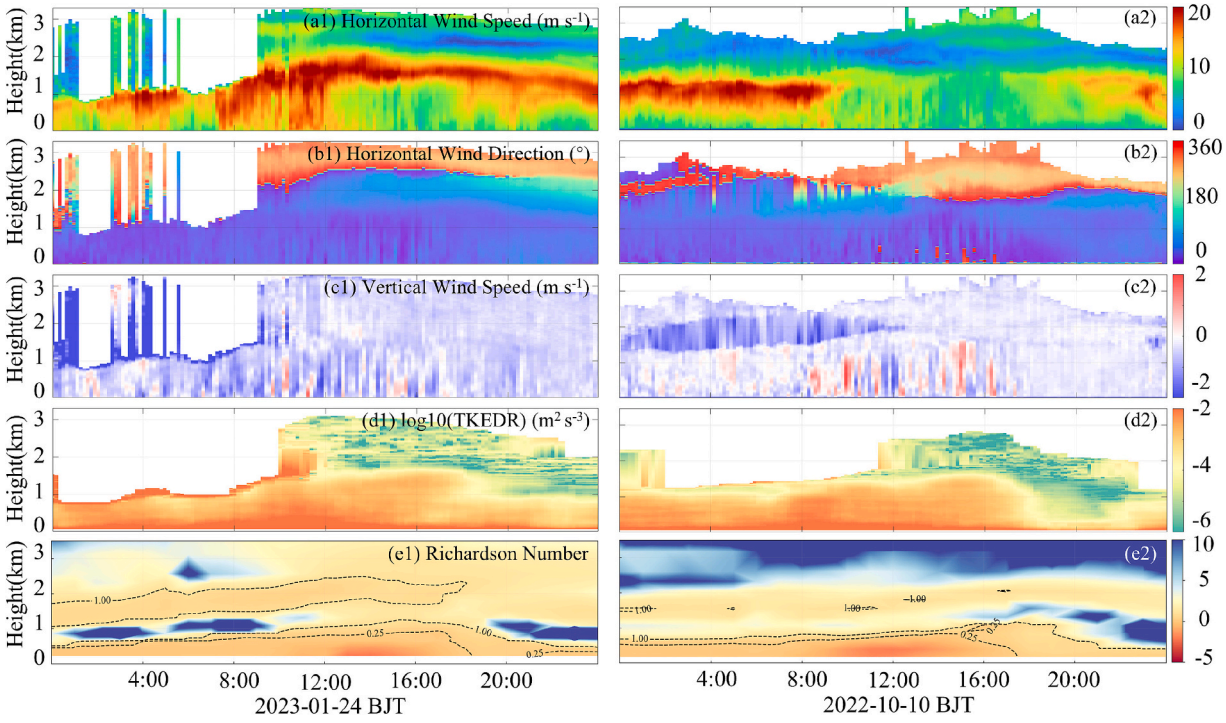

Fig. 7. (a1-e1) The sustained SLLJ case on January 24, 2023; (a2-e2) The interrupted SLLJ case on October 10, 2022. Panels (a-d) show CDWL observations: (a) Horizontal wind speed (m s^{-1}); (b) Horizontal wind direction (°); (c) Vertical wind speed (m s^{-1}); (d) log10(TKEDR) (m^2 s^{-3}). Panels (e) display the gradient Richardson number (Ri) derived from ERA5 reanalysis data.

packed isohypses at 850 hPa over South China from 08:00 to 14:00 BJT, indicating a strong horizontal pressure gradient. At Guangzhou Baiyun International Airport, the 850 hPa wind speed increased from 16.5 m s^{-1} (08,00 BJT) to 18.4 m s^{-1} (11,00 BJT), with cold advection strengthening from -29.5×10^{-5} K s^{-1} to -37.5×10^{-5} K s^{-1}. At 14:00 BJT, the cold advection weakened slightly but the wind speed still maintained a strong intensity of 17.2 m s^{-1}. Concurrently, at 700 hPa (Fig. 8g), a distinct band of positive vorticity was present with a relative vorticity of 5.28×10^{-5} s^{-1} and a wind speed of 14.0 m s^{-1}, corresponding to a cold-frontal shear line across which the wind field shifted from northeasterly to northwesterly, generating cyclonic shear. The coupling of this mid-level shear line with the surface cold front formed a deep baroclinic system, providing sustained dynamic forcing for the SLLJ. Despite some degree of turbulent mixing, the SLLJ was sustained under the combined effect of sustained synoptic-scale momentum transport and its own high core and deep structure, with turbulence exerting a relatively minor overall influence on the jet.

In contrast to most SLLJs that are sustained around noon, a special case of SLLJ interruption was observed on October 10, 2022 (Fig. 7a2-e2). This jet exhibited a core height of 1.14 km, a maximum wind speed of 22 m s^{-1}, and a vertical thickness of 1.64 km, characteristic of the typical deep and strong-wind SLLJ structure. Lidar wind profiles revealed that the jet remained intact during the pre-noon period, with core wind speeds maintaining above 20 m s^{-1}. The JSI calculated from its structural parameters was 0.34, above the sustenance threshold, leading the method to predict a sustained event. However, the observations contradicted this. Around 09:00, along with the development of ascending motion, the jet core wind speed weakened rapidly, generally dropping below 10 m s^{-1} by 14:00, and the jet signature disappeared completely. Meanwhile, analysis of log10(TKEDR) and Ri (Fig. 7d2, e2) reveals that near-surface thermal turbulence gradually developed as the surface warmed, accompanied by a pronounced enhancement of vertical motion throughout the layer, with a maximum updraft of 2.84 m s^{-1} and a mean vertical velocity variance of 0.32 m^2 s^{-2}, both stronger than those during the January 24 event, resulting in intensified turbulence and further enhanced vertical mixing.

Synoptic analysis for that day (Fig. 8d-f) revealed relatively sparsely distributed isohypses at 850 hPa over South China from 08:00 to 14:00 BJT, indicating a weak horizontal pressure gradient. At Guangzhou Baiyun International Airport, the 850 hPa wind speed was 9.9 m s^{-1} (08,00 BJT) and gradually decreased to 8.5 m s^{-1} (11,00 BJT) and 8.0 m s^{-1} (14,00 BJT), with temperature advection fluctuating weakly from -1.9×10^{-5} K s^{-1} to 2.1×10^{-5} K s^{-1}, indicating a marked decay of dynamic forcing. Concurrently, at 700 hPa (Fig. 8h), no prominent positive vorticity band or well-defined shear line was observed, with a relative vorticity of -3.81×10^{-5} s^{-1} and a wind speed of only 6.9 m s^{-1}, reflecting the absence of supporting upper-level dynamic systems. Collectively, synoptic-scale forcing on this day weakened and failed to provide sustained momentum transport to the jet. Under this background, surface heating triggered stronger thermal turbulence than that observed on January 24, enhancing vertical mixing throughout the layer. Combined with the relatively low jet core height and the marked weakening of synoptic-scale forcing, these factors ultimately led to the interruption of the jet.

In the sustained case, strong and persistent synoptic-scale forcing maintained a high jet core with limited turbulent influence. In the interrupted case, weakened synoptic-scale forcing and a lower core height made the jet more susceptible to intense thermal turbulence and vertical mixing triggered by surface heating, leading to rapid dissipation. The JSI, which relies solely on core height and thickness, failed to capture these dynamic and thermal factors, resulting in an incorrect prediction for the interrupted case.

6. Discussion and conclusion

This study utilizes high-resolution observations from a coherent Doppler wind lidar at Guangzhou Baiyun International Airport to analyze the noontime evolution characteristics of LLJs and to develop a discriminant method for their sustenance. The results indicate that the vertical structural characteristics of the jets themselves, particularly

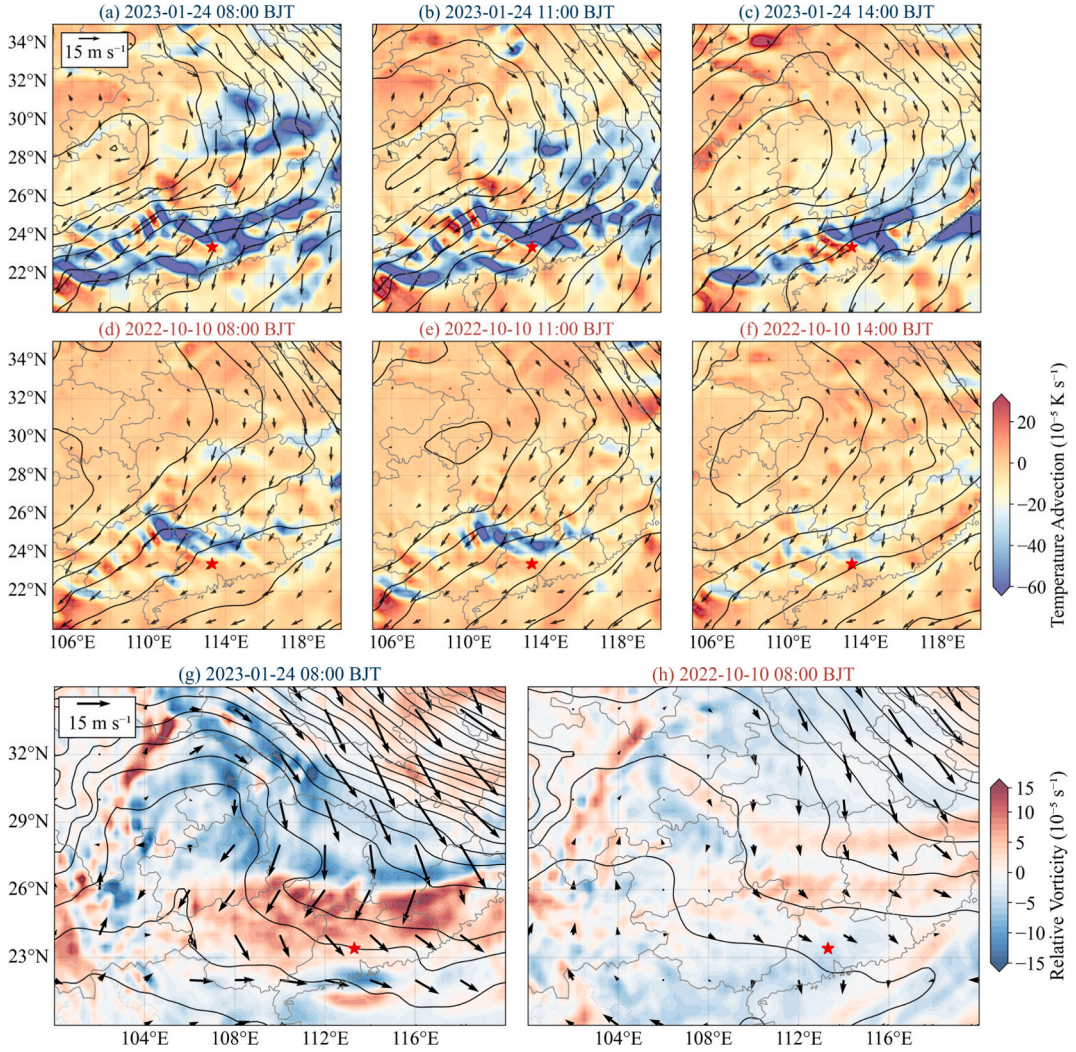

Fig. 8. (a-f) Temperature advection at 850 hPa (shading) superimposed with geopotential height (contours) and wind vectors. (g, h) Relative vorticity at 700 hPa (shading) superimposed with geopotential height (contours) and wind vectors. Red stars denote the location of Guangzhou Baiyun Airport.

core height and thickness, are the key parameters determining their ability to achieve sustenance. Sustained LLJs commonly exhibit features of a high core, thick structure, and strong wind speed, whereas interrupted LLJs display the opposite traits.

Using stratified 5-fold cross-validation, the optimal thresholds for core height and thickness were determined as 0.90 km and 1.15 km, respectively, based on maximizing Youden's J index. A linear weighted Jet Sustenance Index (JSI) was subsequently developed, with optimal weights of 0.64 for core height and 0.36 for thickness, and a JSI threshold of −0.14. The weight distribution in the JSI reflects the distinct physical roles of core height and thickness. Core height determines the vertical position of the jet core relative to daytime thermal turbulence and synoptic-scale momentum supply, acting as the primary control for LLJ sustenance. Thickness enhances structural resistance against turbulent erosion but does not reflect whether the core is exposed to turbulence, thus serving as a secondary modifier. The JSI achieves an accuracy of 84% and an F1-score of 0.86, with the highest precision (93.3%) and specificity (90.5%). Compared with the single core-height threshold, recall increases from 78% to 80% while the FPR drops from 15.3% to 9.5%. Although the 2% gain in recall appears modest, it holds practical significance in aviation safety warnings by reducing the risk of missed sustained LLJ events, while the lower FPR helps avoid unnecessary operational disruptions, achieving a balanced trade-off between alert reliability and efficiency.

Case analysis further reveals the distinct physical mechanisms of the two LLJ types. For BLJs, the sustained case is characterized by low core height but greater thickness and limited turbulence development, while the interrupted case results from upward-developing thermal turbulence reaching the shallow core. For SLLJs, the sustained case features a high core height and is maintained by persistent synoptic-scale forcing, while the interrupted case exhibits a lower core height and occurs when such forcing weakens and strong thermal turbulence develops.

Due to the limited sample size (82 cases), the method's performance was evaluated using stratified 5-fold cross-validation, which mitigates overfitting and provides a robust assessment of generalization capability. The observational data cover only the period from autumn to early spring (October to April), lacking typical summer weather processes. Therefore, the current method is valid for the cold season. Future work will extend the observation period to summer and collect more cases to validate and optimize the JSI for summer conditions. For SLLJ events, key synoptic-scale dynamic and thermodynamic parameters will be selected to construct a composite Synoptic Forcing Index, which will ultimately be incorporated into an optimized JSI model to further enhance operational applicability.

CRediT authorship contribution statement

Yue Liu: Writing – original draft, Methodology, Investigation,

Formal analysis. **Jinlong Yuan:** Writing – review & editing, Supervision, Methodology, Formal analysis, Conceptualization. **Shuo Zhang:** Writing – review & editing, Visualization. **Anning Chen:** Writing – review & editing. **Jiadong Hu:** Writing – review & editing. **Jiawei Qiu:** Writing – review & editing. **Xu Zhou:** Resources, Data curation. **Shuxue Zhou:** Resources, Data curation. **Haiyun Xia:** Visualization, Resources, Data curation. **Zhiyuan Jin:** Resources, Data curation.

Financial support

This study has been supported by the National Natural Science Foundation of China (42405137) and Natural Science Foundation of Jiangsu Province (BK20230434).

Declaration of competing interest

The contact author has declared that none of the authors has any competing interests.

Data availability

Measurement data from the field campaign used in this study are available from the corresponding author upon request (yuanjinlong@nuist.edu.cn).

References

Anuruddhika, M.L.P., Perera, K.K.K.R., Premarathna, L.P.N.D., Pathiranage, T.H.W., Weerasinghe, V.P.A., 2025. Development of a novel slope-integrated drought index (SIDI) for comprehensive drought assessment. Theor. Appl. Climatol. 156, 322. https://doi.org/10.1007/s00704-025-05563-3.

Banakh, V.A., Smalikho, I.N., 2018. Lidar studies of wind turbulence in the stable atmospheric boundary layer. Remote Sens. 10, 1219. https://doi.org/10.3390/rs10081219.

Banakh, V.A., Smalikho, I.N., Falits, A.V., 2021. Estimation of the height of the turbulent mixing layer from data of doppler lidar measurements using conical scanning by a probe beam. Atmos. Meas. Tech. 14, 1511–1524. https://doi.org/10.5194/amt-14-1511-2021.

Banta, R.M., Pichugina, Y.L., Brewer, W.A., 2006. Turbulent velocity-variance profiles in the stable boundary layer generated by a nocturnal low-level jet. J. Atmos. Sci. 63, 2700–2719. https://doi.org/10.1175/JAS3776.1.

Blackadar, A.K., 1957. Boundary layer wind maxima and their significance for the growth of nocturnal inversions. Bull. Am. Meteor. Soc. 38, 283–290. https://doi.org/10.1175/1520-0477-38.5.283.

Bonner, W.D., 1968. Climatology of the low level jet. Mon. Wea. Rev. 96, 833–850. https://doi.org/10.1175/1520-0493(1968)096%253C0833:COTLLJ%253E2.0.CO;2.

Borna, N.J., Rahman, Md.H., 2024. Evaluating the degree of cloudiness using machine learning techniques based on different atmospheric conditions. Theor. Appl. Climatol. 155, 7193–7222. https://doi.org/10.1007/s00704-024-05062-x.

Breiman, L., 2001. Random forests. Mach. Learn. 45, 5–32. https://doi.org/10.1023/A:1010933404324.

Chan, P.W., Hon, K.K., Li, Q.S., 2020. Low-level windshear associated with atmospheric boundary layer jets – case studies. ATM 34, 461–490. https://doi.org/10.20937/ATM.52866.

Chen, Y.-L., Chen, X.A., Zhang, Y.-X., 1994. A diagnostic study of the low-level jet during TAMEX IOP 5. Mon. Weather Rev. 122, 2257–2284. https://doi.org/10.1175/1520-0493(1994)122%253C2257:ADSOTL%253E2.0.CO;2.

Choi, M.-H., Lee, Y.-H., 2012. Characteristics of nocturnal low-level jets over ulsan airport. Asia-Pacific J. Atmos. Sci. 48, 181–189. https://doi.org/10.1007/s13143-012-0018-2.

Cohen, J., 1977. CHAPTER 1 - the concepts of power analysis. In: Cohen, J. (Ed.), Statistical Power Analysis for the Behavioral Sciences. Academic Press, pp. 1–17. https://doi.org/10.1016/B978-0-12-179060-8.50006-2.

Darby, L.S., Allwine, K.J., Banta, R.M., 2006. Nocturnal low-level jet in a mountain basin complex. Part II: transport and diffusion of tracer under stable conditions. J. Appl. Meteorol. Climatol. 45, 740–753. https://doi.org/10.1175/JAM2367.1.

Ding, J., Ren, Y., Zhang, H., Chang, H., Hu, Z., Liang, J., Zhang, K., Wang, S., Cao, X., Tian, P., Zhang, L., 2025. Mechanism of turbulence structure evolution in the nocturnal boundary layer during the interaction of low-level jet and internal gravity waves: based on full boundary layer turbulence observations. JGR Atmos. 130, e2024JD042106. https://doi.org/10.1029/2024JD042106.

Dong, F., Zhi, X., Zhang, L., Ye, C., 2021. Diurnal variations of coastal boundary layer jets over the northern South China Sea and their impacts on diurnal cycle of rainfall over southern China during the early-summer rainy season. Mon. Weather Rev. 149, 3341–3363. https://doi.org/10.1175/MWR-D-20-0292.1.

Du, Y., Chen, G., 2018. Heavy rainfall associated with double low-level jets over southern China. Part I: ensemble-based analysis. Mon. Weather Rev. 146, 3827–3844. https://doi.org/10.1175/MWR-D-18-0101.1.

Du, Y., Chen, G., 2019. Climatology of low-level jets and their impact on rainfall over southern China during the early-summer rainy season. J. Climate 32, 8813–8833. https://doi.org/10.1175/JCLI-D-19-0306.1.

Du, Y., Zhang, Q., Ying, Y., Yang, Y., 2012. Characteristics of low-level jets in Shanghai during the 2008-2009 warm seasons as inferred from wind profiler radar data. J. Meteorol. Soc. Jpn. 90, 891–903. https://doi.org/10.2151/jmsj.2012-603.

Holton, J.R., 1967. The diurnal boundary layer wind oscillation above sloping terrain. Tellus 19, 199–205. https://doi.org/10.1111/j.2153-3490.1967.tb01473.x.

Hu, X.-M., Klein, P.M., Xue, M., Lundquist, J.K., Zhang, F., Qi, Y., 2013. Impact of low-level jets on the nocturnal urban heat island intensity in Oklahoma City. J. Appl. Meteorol. Climatol. 52, 1779–1802. https://doi.org/10.1175/JAMC-D-12-0256.1.

Li, J., Chen, Y.-L., 1998. Barrier jets during TAMEX. Mon. Weather Rev. 126, 959–971. https://doi.org/10.1175/1520-0493(1998)126%253C0959:BJDT%253E2.0.CO;2.

Li, X., Du, Y., 2021. Statistical relationships between two types of heavy rainfall and low-level jets in South China. J. Climate 34, 8549–8566. https://doi.org/10.1175/JCLI-D-21-0121.1.

Li, L., Shao, A., Zhang, K., Ding, N., Chan, P.-W., 2020. Low-level wind shear characteristics and lidar-based alerting at Lanzhou Zhongchuan International Airport, China. J. Meteorol. Res. 34, 633–645. https://doi.org/10.1007/s13351-020-9134-6.

Luo, Y., Du, Y., 2025. Moisture sources and sinks of low-level jets in south China: a backward and forward trace model approach. J. Climate 38, 2641–2658. https://doi.org/10.1175/JCLI-D-24-0200.1.

Madougou, S., Saïd, F., Campistron, B., Cheikh, F.K., 2013. Low level jet wind shear in the Sahel. JERA 11, 1–10. https://doi.org/10.4028/www.scientific.net/JERA.11.1.

Miao, J., Zhu, W., 2022. Precision–recall curve (PRC) classification trees. Evol. Intel. 15, 1545–1569. https://doi.org/10.1007/s12065-021-00565-2.

Miao, Y., Guo, J., Liu, S., Wei, W., Zhang, G., Lin, Y., Zhai, P., 2018. The climatology of low-level jet in Beijing and Guangzhou, China. JGR Atmos. 123, 2816–2830. https://doi.org/10.1002/2017JD027321.

Parish, T.R., Oolman, L.D., 2010. On the role of sloping terrain in the forcing of the great plains low-level jet. J. Atmos. Sci. 67, 2690–2699. https://doi.org/10.1175/2010JAS3368.1.

Rife, D.L., Pinto, J.O., Monaghan, A.J., Davis, C.A., Hannan, J.R., 2010. Global distribution and characteristics of diurnally varying low-level jets. J. Climate 23, 5041–5064. https://doi.org/10.1175/2010JCLI3514.1.

Schisterman, E.F., Faraggi, D., Reiser, B., Hu, J., 2008. Youden index and the optimal threshold for markers with mass at zero. Stat. Med. 27, 297–315. https://doi.org/10.1002/sim.2993.

Shu, Z.R., Li, Q.S., He, Y.C., Chan, P.W., 2018. Investigation of low-level jet characteristics based on wind profiler observations. J. Wind Eng. Ind. Aerodyn. 174, 369–381. https://doi.org/10.1016/j.jweia.2018.01.035.

Song, J., Liao, K., Coulter, R.L., Lesht, B.M., 2005. Climatology of the low-level jet at the southern great plains atmospheric boundary layer experiments site. J. Appl. Meteorol. 44, 1593–1606. https://doi.org/10.1175/JAM2294.1.

Stensrud, D.J., 1996. Importance of low-level jets to climate: a review. J. Climate 9, 1698–1711. https://doi.org/10.1175/1520-0442(1996)009%253C1698:IOLLJT%253E2.0.CO;2.

Storm, B., Dudhia, J., Basu, S., Swift, A., Giammanco, I., 2009. Evaluation of the weather research and forecasting model on forecasting low-level jets: implications for wind energy. Wind Energy 12, 81–90. https://doi.org/10.1002/we.288.

Su, L., Lu, C., Yuan, J., Wang, X., He, Q., Xia, H., 2024. Measurement report: the promotion of the low-level jet and thermal effects on the development of the deep convective boundary layer at the southern edge of the Taklimakan Desert. Atmos. Chem. Phys. 24, 10947–10963. https://doi.org/10.5194/acp-24-10947-2024.

Wang, L., Qiang, W., Xia, H., Wei, T., Yuan, J., Jiang, P., 2021. Robust solution for boundary layer height detections with coherent Doppler wind lidar. Adv. Atmos. Sci. 38, 1920–1928. https://doi.org/10.1007/s00376-021-1068-0.

Xia, H., Chen, Y., Yuan, J., Su, L., Yuan, Z., Huang, S., Zhao, D., 2024. Windshear detection in rain using a 30 km radius coherent Doppler wind lidar at mega airport in plateau. Remote Sens. 16, 924. https://doi.org/10.3390/rs16050924.

Yan, Y., Cai, X., Wang, X., Miao, Y., Song, Y., 2021. Low-level jet climatology of china derived from long-term radiosonde observations. JGR Atmos. 126, e2021JD035323. https://doi.org/10.1029/2021JD035323.

Yuan, J., Xia, H., Wei, T., Wang, L., Yue, B., Wu, Y., 2020. Identifying cloud, precipitation, windshear, and turbulence by deep analysis of the power spectrum of coherent Doppler wind lidar. Opt. Express 28, 37406. https://doi.org/10.1364/OE.412809.

Zhang, D.-L., Zhang, S., Weaver, S.J., 2006. Low-level jets over the mid-Atlantic states: warm-season climatology and a case study. J. Appl. Meteorol. Climatol. 45, 194–209. https://doi.org/10.1175/JAM2313.1.

Zhang, H., Wu, S., Wang, Q., Liu, B., Yin, B., Zhai, X., 2019. Airport low-level wind shear lidar observation at Beijing capital international airport. Infrared Phys. Technol. 96, 113–122. https://doi.org/10.1016/j.infrared.2018.07.033.

Zheng, E., Du, Y., Luo, Y., Zhang, Q., Chen, G., Su, L., Kong, H., 2026. Two types of low-level jets in China during the warm season: observational climatology from radiosonde data. Atmos. Ocean. Sci. Lett., 100791 https://doi.org/10.1016/j.aosl.2026.100791.

Zhou, C., Chen, G., Du, Y., Su, L., 2026. Double low-level jets over South China in the warm season: diversity and impacts. J. Geophys. Res. Atmos. 131, e2025JD045497. https://doi.org/10.1029/2025JD045497.